FULL RESEARCH ARTICLE

Application of interlaminar shear strength and finite element modeling for failure analysis of 3D printed continuous fiber-reinforced composites

Yu-Chao Shih[1] · Mahmoud Mohamed[1] · Jun Ge[1] · Subhayu Sen[2] · Selvum Pillay[1] · Haibin Ning[1]

Abstract

Continuous fiber-reinforced plastic composite materials are being increasingly used in material extrusion additive manufacturing, typically fused filament fabrication, because it enables unprecedented freedom to manufacture high-performance parts on demand and on-site. Interlayer weaknesses of continuous fiber-reinforced plastic composites made by additive manufacturing need to be addressed to assure the structural integrity of a design that is inherently anisotropic, commonly determined by characterization of interlaminar shear strength. In this study, interlaminar shear strength of 3D-printed continuous fiber-reinforced plastic composites was characterized with a single-lap joint specimen. It was observed that the interlaminar shear strength and failure mode changes as a function of the fiber orientation. The layup sequences were found to affect the stress distribution over the joint area, causing non-tensile failure regarding the eccentric load. The bonding quality data were compared to finite element analysis results to map the effective load transfer to the interlaminar area between each printed laminated structure. Stress distribution of the 3D-printed laminated structure under tension loading can be complex, and the results from such tests can be misinterpreted. Based on the present investigation, it is recommended that the layup design should incorporate a balanced stiffness to take advantage of continuous fiber reinforcement.

Keywords Interlaminar shear strength · Single-lap joint · Continuous fiber-reinforced plastic · Additive manufacturing · Fused filament fabrication · Finite element analysis

1 Introduction

Additive manufacturing (AM) has demonstrated the potential to revolutionize manufacturing and enable the deployment of novel materials for advanced applications [1]. AM technology enables performance-driven design [2–4] and an integration-friendly environment to aid the implementation of novel materials into new applications, such as aerodynamically enhanced jet engines printed with laser powder bed AM [5], tissue engineering using a hybrid bioprinting method [6], and the unmanned vehicle made of FFF composites [7, 8], to name a few. Fused filament fabrication (FFF) is one of the most popular material-extrusion AM technology, which is capable of utilization of an array of filament feedstock, including continuous fiber-reinforced plastic (CFRP), to form solid object based on its layer-by-layer extrusion process. CFRP composites possess high specific strength and modulus. Continuous fiber reinforcement (CFR) [9–12] technology is the frontrunner for additively manufactured composites for their simplicity, flexibility of architecture design, and tailored performance. AM of CFR utilizes a dual extrusion system to deposit multiple materials alternatively, one of which is continuous fiber-reinforced plastic composite.

In spite of the advantages cited above, due to the layered deposition, the main shortcoming of the AM process is the systematic defects embedded within the laminas and interfacial regions [15], as illustrated in Fig. 1. The typical void content of a 3D-printed CFRP is reported in the literature to be around 5% [12, 16]. Insufficient consolidation could cause poor adhesion or interfacial bonding issues [17]. This

✉ Haibin Ning
ning@uab.edu

1 Department of Mechanical and Materials Engineering, Materials Processing and Applications Development (MPAD) Center, University of Alabama at Birmingham, Birmingham, AL 35294, USA

2 Sev1Tech LLC, Space Science and Engineering, 6703 Odyssey Dr NW #103, Huntsville, AL 35806, USA
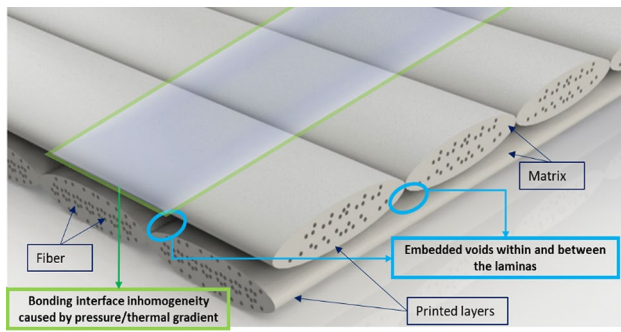
Fig. 1 Physical defects in continuous fiber-reinforced plastic composite fabricated with extrusion-based additive manufacturing (adapted from [13, 14])

is a direct manifestation of the gradient solidification during the extrusion-deposition procedure. Based on the inherent interfacial defects within the structure, the primary composite failure modes are shown in Fig. 2. The similarities of these failure modes between conventional composites and AM structures have been previously discussed elsewhere [13, 18, 19]. The simplest criteria to predict such failure is the interlaminar shear strength (ILSS), prescribing the failure would occur upon a critical threshold is reached. One of the standard ILSS characterization methods is the short beam shear (SBS) test, which applies a flexural load on a thick specimen to monitor the shear strength of the neutral layer upon delamination. Many authors have investigated the ILSS of 3D printed composites with SBS samples as a function of fiber type, layer thickness, and fiber orientations [20–22]. SBS test results from the literature suggest a low ILSS value for 3D-printed composites compared to commercial composites, concluding that the embedded voids are the primary contributing factor. Iragi et al. [16] went one

step further to characterize the mechanical properties at the lamina level, including mode I and mode II fracture toughness. The inefficiency of the reinforcement was evidenced by several studies [20, 22–24] showing that ILSS and tensile properties do not increase proportionally with higher fiber volume fraction. Despite the apparent use of the SBS test for quantifying ILSS, the method is limited to unidirectional and symmetrical ply.

Characterization of the bonding quality of an adhesive-bonding system is highly specialized as load transfer between dissimilar materials and bonding geometry can be nontrivial and resulting in complex stresses. Single-lap joint (SLJ) is one of the basic bonding geometries and are widely used to compare adhesion strength for varying conditions, due to its simplicity in design and application [26]. Composed of two lapped-body bonded with a layer of adhesive [27], SLJ originated from the necessity of combining assemblies or structural reinforcement. Despite the simplicity of manufacturing the testing specimens, caution must be exercised to prevent misuse of the SLJ stress as allowable design stress because of the complex stress in the system [28]. Milestone SLJ stress field analysis includes the Goland and Reissner analysis, accounting for load eccentricity and beam bending [29] and Volkersen's differential shear treatment [30]. A representative sandwich element of two adherend bodies and a layer of adhesives is usually used in the analysis based on the formulations of plate theories [31]. Analytical models for bonded joints were reviewed, implemented, and compared by da Silva [32, 33] as to provide an accurate prediction of SLJ strength. A lap shear test is usually conducted to examine the interlaminar bonding of adhesives between bonded surfaces on a quantitative and comparative basis [27, 29, 34]. Other than the intended use of functional evaluation of a designed bonded joint, the growing popularity of using

Fig. 2 Typical failure modes of conventional additively manufactured continuous fiber-reinforced plastic composites (Adapted from [25])

Interface delamination

Fiber failure

Interply cracking
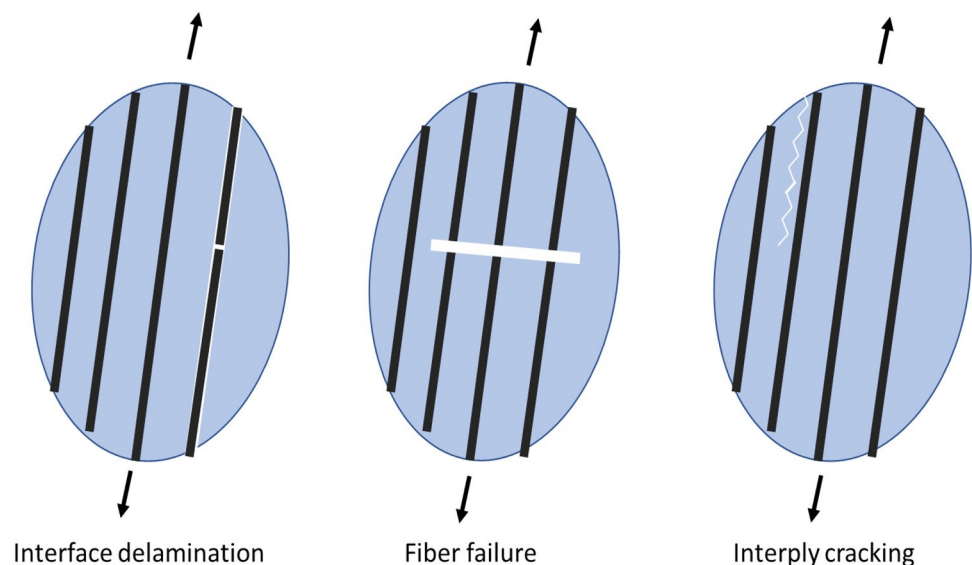
the SLJ specimen for characterizing the interfacial bonding strength of fiber-reinforced laminate or 3D-printed structure has been discussed elsewhere in the literature [35–40]. A considerable sum of analytical treatments for SLJ specimens is available to be implemented in the analytical and numerical analysis [32, 41]. However, the nature of the prescribed adhesive thickness and mostly plane stress simplification does not necessarily apply to AM FRP specimens due to its complex laminate blending profile and structural integrity within the laminas. From the material standpoint, the AM FRP differs from conventional beam composition as it is highly anisotropic and possess less integrity than of the beam.

This study aims to develop a novel methodology to analyze the fracture behavior of the SLJ specimen in relation to continuous fiber orientation and stacking sequences. The coupling of voids and the inherent anisotropic nature of an AM composite material can further complicate its structural integrity assessment. It is demonstrated that a combination of experimental results and a simulation approach can be used to optimize the performance. Interlaminar bonding quality assessment of AM FRP composites, including unbalanced laminated SLJ specimens, was further advanced using a physics-based observation of the failure of SLJ specimens. Finite element analysis (FEA) was implemented to analyze the stress distribution profile over the lapped length accounting for geometric deflection on the laminated SLJ specimens. The fracture morphologies and load were recorded and correlated to the stress field results from the simulation.

2 Materials and methods

2.1 Materials and equipment

All CFRP samples were fabricated with the Mark Two 3D printer (Markforged, MA, USA). Mark Two is a desktop composite 3D printer using the principle of material extrusion-based additive manufacturing technologies of FFF and continuous fiber reinforcement (CFR). Onyx, a chopped carbon fiber reinforced PA6 composite filament, and continuous carbon fiber (CCF) composite filament were used to manufacture specimens. Printing parameters were pre-set at a printing temperature of 270 °C on both extrusion outlets and a layer height of 0.125 mm. A 100% infill matrix, labeled as solid infill, was chosen to fabricate the specimen in this study based on a rectangular infill pattern of alternate $+45°/-45°$ raster angle. The specimen geometry was made with a commercial CAD software Solidworks 2021 (Solidworks, Dassault Systems, Tennessee). Tensile tests following the procedure specified by ASTM D3039 were used to get a baseline property for composites made from 100% Onyx and 100% continuous carbon fiber composite

filaments, respectively. All mechanical tests were conducted on an MTS 810 system with a 2 kN load cell. The result would be used in further analysis to generate baseline lamina parameters in FEA.

2.2 Single-lap shear test

All SLJ specimens were manufactured with the Mark Two 3D printer. The specimens would be subjected to a 2 mm/min constant crosshead rate until failure, for which the load–displacement relationship was recorded. The maximum length of the overlapping area to assure failure at the bonded joint region was determined by the equation [42],

$$L < F_{ty}T/\tau \tag{1}$$

in which L is the overlap length, T is the adherend thickness, F_{ty} is the yield strength of the adherend, and τ is 50% of the estimated average shear strength in the bonded joint [43]. The overlapped length of $L = 6.4$ mm was conservatively chosen for all configurations to avoid undesired tensile failure on the adherend based on the properties from the literature [16] and this study. The SLJ specimen are dimensionally symmetric and each adherend beam is dimensioned at $82.55 \times 12.7 \times 3$ mm with an overlapping area of 6.4×12.7 mm, as shown in Fig. 3a. Figure 3b shows the engineering drawing of the specimen with detailed dimensions. The formulation suggested by ASTM standard to calculate the single-lap joint strength considers the load fully applied on a simplified interfacial area over the bonded adhesive joint [28, 42, 43]. Under this context, the average shear strength is:

$$\tau = \frac{P}{bl} \tag{2}$$

where P is the load at failure, b is the width of the joint, and l is the single-lap length. Table 1 shows the fiber layout orientation and purposes of each SLJ specimen design variant. Three specimens were printed and tested for each variant. Designed configurations are summarized below in Fig. 4. Additional baseline samples B1 for pure Onyx and B2 for 4-ply Onyx interface reinforced with four 0°-ply outside of the bonded joint were configured. B1 and B2 compare the SLJ strength of the Onyx interface with and without stiffener plies outside of the load path. Each specimen was printed with an automatically generated support structure under the upper adherend. The support structure was removed before being tested.

2.3 Fracture surface analysis

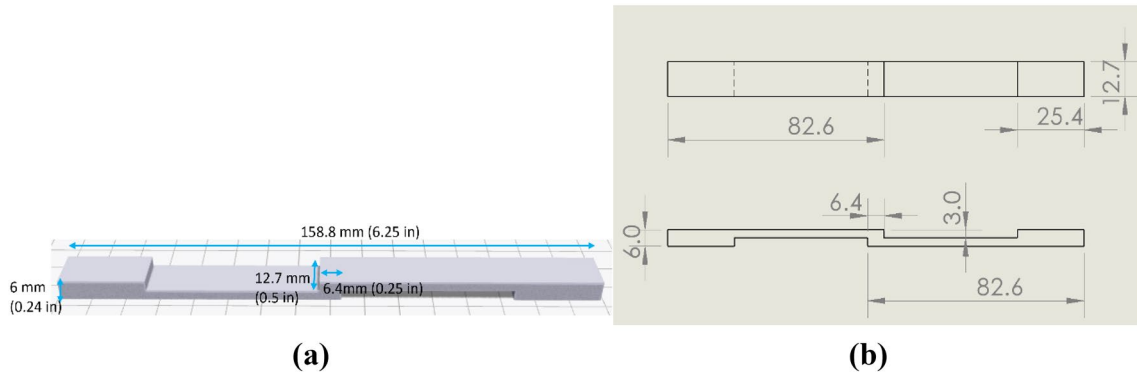Morphological observation of the fracture surface is the centerpiece of identifying the onset of the fracture and the

Fig. 3 Single-lap joint specimen design, **a** Isometric view, **b** Engineering drawing. (Unit: mm)

Table 1 Experiment design on single-lap joint shear test for FRP composites

Designation	Purpose	Description
M	Evaluate the effect of fiber layups between interfacial bonded areas	Orientation of a 4-ply laminated structure Five different layer sequences at the lap joint: (0°–0°; 0°–90°; 90°–90°; 0°–45°; 45°–135°)
N	Evaluate the effect on the extensional stiffness and asymmetry on adherend beam	Orientation of an 8-ply laminated structure Three different layer sequences at the lap joint: (0°/45°–135°/0°; 0°/90°–90°/0°; 0°/90°–0°)
O	Evaluate the effect of a buffer layer between unidirectional CF reinforcement	Orientation of 1 or 2 plies between the 4-ply 0° CF Three different layer sequences at the lap joint: (45°; 90°; Onyx-45°)
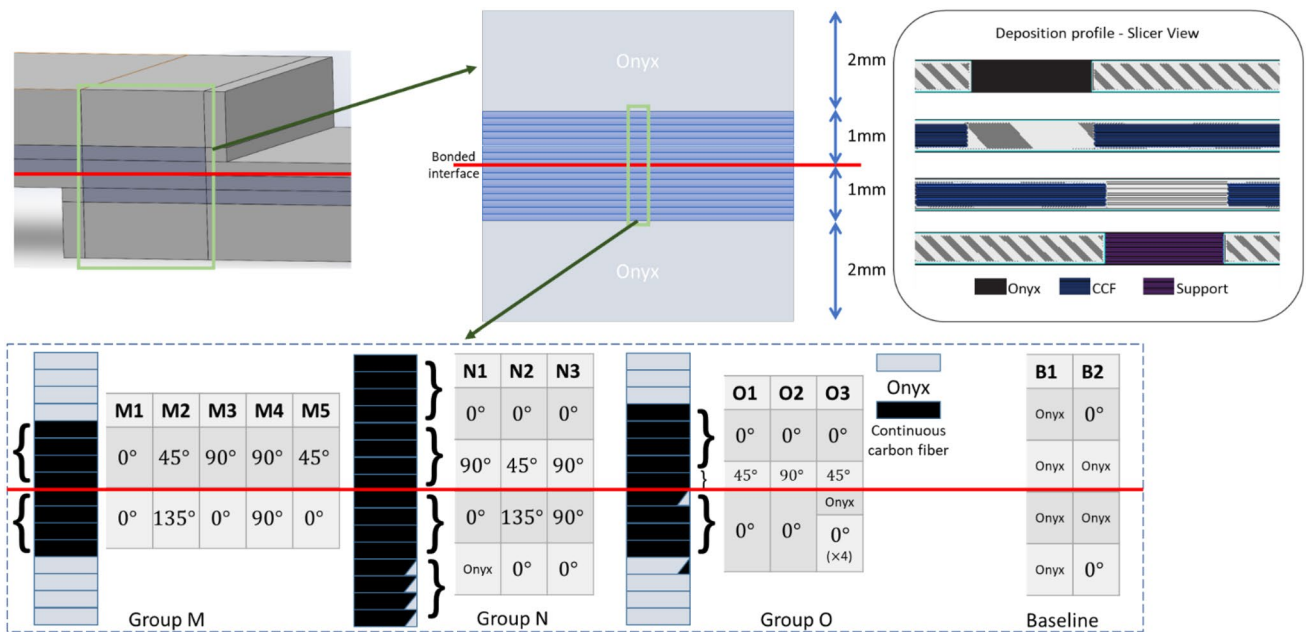
Fig. 4 Schematics of fiber layout sequences over the bonded joint for the SLJ specimen design

failure mode itself. The structural integrity of an interlaminar area between two adherends can be assessed by matching a specific fracture pattern defined by the corresponding type of stress. Failure mode recognition of the AM composite SLJ samples was performed with a modified figure similar to the ASTM D5573 (Standard Practice for Classifying Failure Modes in Fiber-Reinforced-Plastic (FRP) Joints) [44]. Images of the fracture surface specimens were taken with DinoLite AM3111 digital microscopy with 0.3-megapixel image resolution. Side images were also taken to identify the location of the fracture onset. The fracture mode can be a manifestation of a combination of stresses, namely longitudinal tensile stress, through-thickness peel stress, and interlaminar shear stress.

2.4 Finite element analysis

Finite element analysis (FEA) has been used extensively in modeling laminated composites to provide accurate stress fields at a laminate level [45]. Using an engineering FEA suite, ANSYS professional 2022R1, a three-dimensional FEA was conducted to simulate the stress field of the SLJ specimen. Material properties were calibrated with the tensile test results, such that the simulation of nonlinear Onyx softening behavior was permitted throughout straining. The ten-percent-rule [46] was used as an approximation tool for required out-of-plane properties, assuming the transverse modulus as one-tenth of the longitudinal modulus. The solid model was constructed with geometrical detail including all walls and other configured features. The laminated composition was configured with the ANSYS Composites PrePost (ACP) using orthotropic material properties and element SOLID185. SOLID185 is nominally known as a homogeneous brick element, which has eight nodes, and each node has 3 degrees of freedom (DoF). The enforced load of failure on each configuration was set on one side of the adherend and fixed support on the other. Non-slide boundary conditions were applied to the tabbed surfaces to constrain the models as in the experiment. The interfaces were assumed to be perfectly bonded since the interlaminar shear strain is minor compared to the extensional strain of the adherend until joint failure by sudden debonding. Twenty-four sub-steps were implemented with a 6 s pseudo-time to capture the nonlinearity of the model. The through-thickness peel stress, tensile stress, and interlaminar shear stress were recorded, plotted, and compared to the experimental data. A set of convergence studies was conducted to assure sufficient mesh discretization with the prescribed element size [47] to avoid stress singularity and improve precision. Trials have been conducted with element sizes of 8, 4, 3, 2, 1.2, 0.8, 0.5, 0.4, 0.2, and 0.15 mm within the lamina, while the thickness remains unchanged. It was determined that the element size of 0.2 mm is sufficient for a valid result.

3 Result and discussion

3.1 Feedstock material characterization

The tensile specimen was dimensioned at $152 \times 12.7 \times 6.4$ mm, with the gage length set to 76.2 mm. The outer wall layers of the CCF specimen have been removed to achieve the composition of 100% CCF filaments. The characterized tensile modulus and strength are shown in Table 2. The nonlinear plasticity on the stress–strain relationship of the matrix Onyx was calibrated and will be put into the simulation as material properties. The elastic and plastic segments of the tensile stress–strain data of Onyx were input into the model to develop proper responses of the AM printed samples.

Each SLJ specimen was measured before the tests to assess the dimensional deviation. The width and length of the overlapped area were recorded and compiled. The average dimensional deviation of the overlapping area was found to be minimal (around 2%).

3.2 Lap shear results

SLJ results from all M, N, and O specimens were summarized in Fig. 5. The baseline SLJ strength of pure Onyx specimen B1 and stiffened Onyx B2 are also included. Group M data show the highest shear stress for 0°–0° (M1) at 28.5 MPa, and the lowest at 10.2 MPa for 90°–90° specimens. The peeling force on the edge of the joint induced by beam bending under tensile load weakens the structural integrity of the 3D-printed single-lap joint, resulting in a 12.3% lower strength of 25 MPa for 0°–45° (M5), a 48.5% lower strength of 14.7 MPa for 0°–90° (M3), 53.7% lower strength of 13.2 MPa for 45°–135° (M2), and a 64.2% lower strength of 10.2 MPa for 90°–90° (M4). It is observed that although the presence of an imbalanced beam of greater stiffness would induce additional bending, the overall structural strength of those M3/M5 is still larger than those without 0° plies (M2, M4).

All group M results were plotted in Fig. 6. The 0°–0° specimen shows the lowest strain to failure while the 90°–90° have the highest strain-to-failure. The other configurations have the strain-to-failure in between. It was found that a lower strain-to-failure showed the highest failure load,

Table 2 Tensile test results for continuous fiber-only and Onyx-only 3D-printed composites

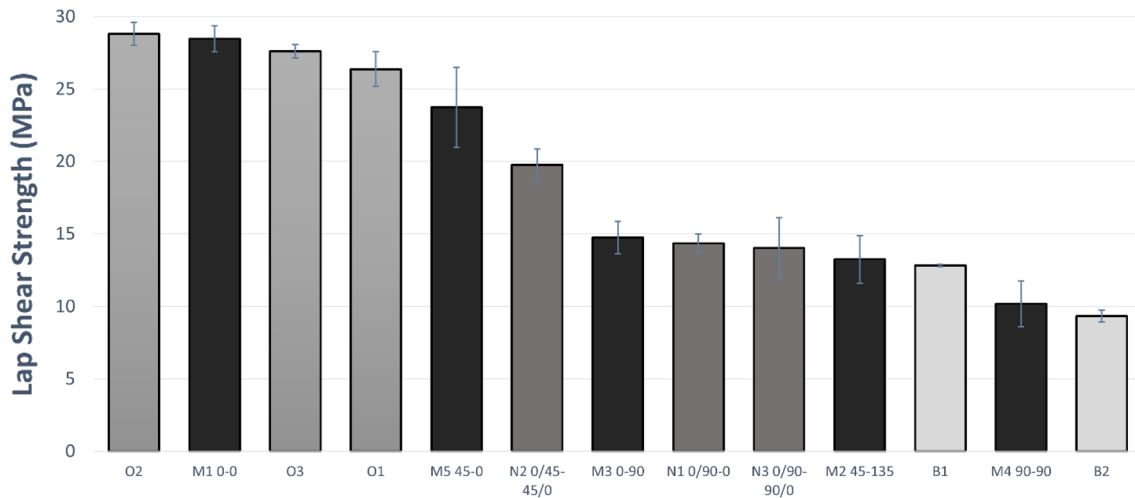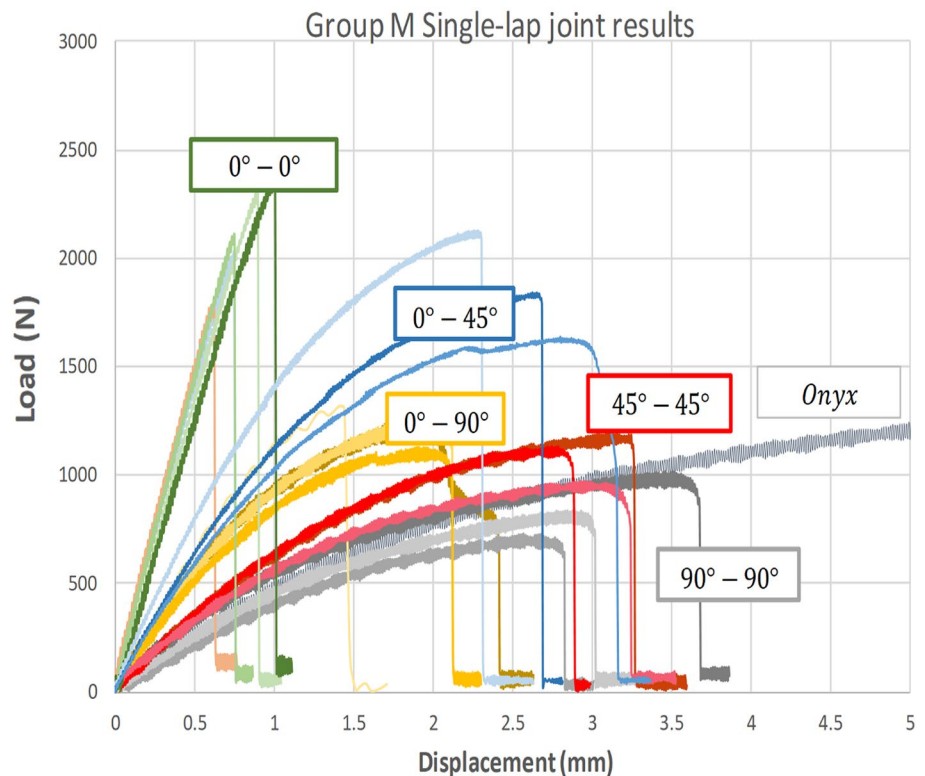| Material	Modulus (GPa)	Strength (MPa)
Laminated carbon fiber	66.5 ± 0.7	811.0 ± 18
Laminated Onyx	1.26 ± 0.1	34.4 ± 1.6

Fig. 5 Comparison of all SLJ results by group

Fig. 6 Load–displacement curves of all group M results with Onyx baseline

and a higher strain-to-failure showed a lower failure load. The relationship implies the bonded structure could bear more load with a higher beam modulus by reducing load eccentricity. The ILSS from the literature suggests ~ 30 MPa for CF-Onyx composites with the SBS test [16], which is consistent with the result in this study. The SLJ result gives a more conservative estimation because of the presence of additional bending from the geometry's free edges. The concentration over the free edges was alleviated by the enclosure

walls and layered structures. The enclosure constituted of the base material was configured to protect the integrity of the samples as well as prevent failure on free edges by stress concentration permitting strain energy to be released by straining. The mechanism is similar to a mixed-adhesive joint (MAJ) [48, 49], for which the adhesively bonded lapped region consists of a rigid adhesion in the middle section and two flexible adhesion on the sides. The effect of eliminating the excessive interlaminar shear stresses on the

unsupported free edges under tensile loading was evident in this study and is consistent with that stated in [50]. Group N shows that the N2 specimen has an average strength of 19.5 MPa, which is 35% higher than the 14.4 MPa of the N3 specimen. The failure mode of mixed intralaminar failure on N3 stiffened 90°–90° also differs from the cohesive interlaminar debonding on a stiffened 45°–135 of N2. The result confirms that the 90° layer is more susceptible to a composite shear-peel loading. Although the N1 and N3 differ by four layers of unidirectional 0° layer, the resulting SLJ shear strength does not result in a significant difference. It is reasonable as the fiber orientation around the section of stiffness centroid is identical and prone to a lamina failure on the 90° layer.

Group O result shows the effect of an additional off-axis buffer layer on specimens with similar structural bending stiffness. O2 specimen has the highest strength of 28.8 MPa for the additional 90° layer gives extra flexibility on the stress-concentrated x direction. It is followed by 27.6 MPa for the O3 specimen that was buffered with a 45°-Onyx bilayer over the interlaminar centroid region, and the lowest of 26.4 MPa for O1, which has an additional 45° layer. The comparable SLJ strength on group O result confirms the previous assumption that structural stiffness in the loading direction is the primary factor in SLJ strength. The additional buffer layer in the O specimens does not improve the shear strength significantly compared to the M1 0°–0°. The boxplot on groups M and N results are shown in Fig. 7, which also displays the variability on each configuration. The similarity has been found in the plateaued trend in M3-N1-N3 for the presence of the 0–90 interface. It is evident that the reinforced 0°–90° configuration is prone to lamina failure on the 90° layer. Comparing these two groups

shows that the fiber orientation type is the most important parameter, followed by the beam stiffness. The interval plot for the 95% confidence interval (CI) result of all continuous FRP specimens is listed in Fig. 8.

The result shows that as the stiffness of the weaker adherend increases, the SLJ strength increases drastically. The greater lap shear strength was observed when both adherends are of higher longitudinal stiffness. Significant peel effect was observed on those with higher bending angles, which could be subsequently exacerbated by low flexural stiffness on symmetrical samples and the degree of stiffness difference between two adherends on asymmetrical samples. From the SLJ strength in descending order 0–0 (M1) > 0–45 (M5) > 45–135 (M3) > 0–90 (M2) > 90–90 (M4), it can be surmised that an important parameter that affects the SLJ strength is the interface type at the interlaminar region. The 0° layers near the stiffness centroid can decrease load eccentricity with the increased flexural stiffness, resulting in higher effective shear stress on the beam. In contrast, if the stiffness centroid has lower flexural resistance, the bending effect would result in greater peel stress. It was also evidenced in the B2 samples, with the lowest SLJ strength resulting from delamination due to off-axis load that causes peel-dominant delamination. It is concluded that the stress composition resulting from the load situation would play an essential role in the structural assessment.

3.3 Fracture analysis

The primary fracture types of the SLJ samples are summarized in Fig. 9. Type A shows a shear-dominant failure mode as the fracture propagates through the interlaminar region. Type B is associated with concentrated peel stress along the

Fig. 7 Result of SLJ strength of continuous FRP composites on groups M and N
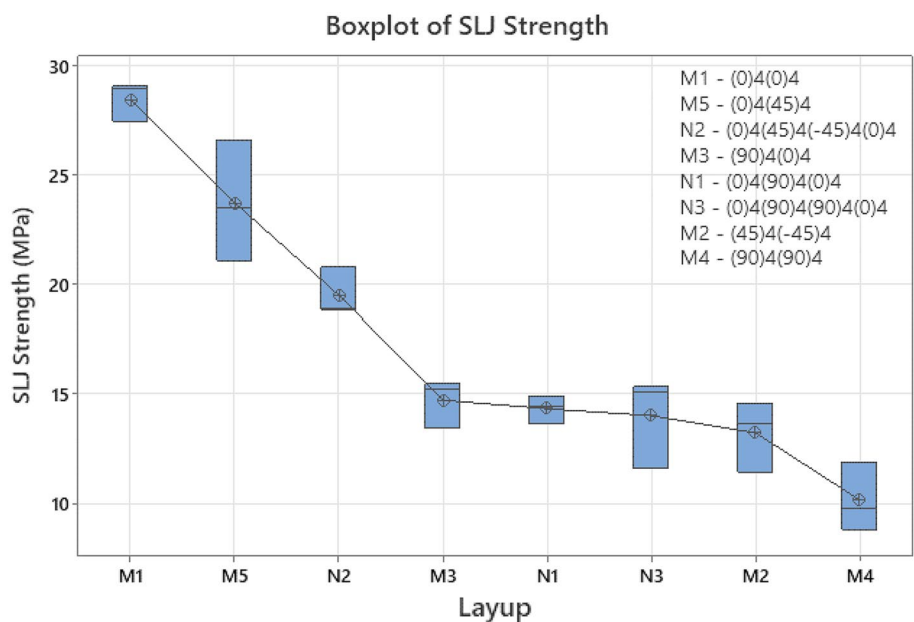

Boxplot of SLJ Strength

M1 - (0)4(0)4
M5 - (0)4(45)4
N2 - (0)4(45)4(-45)4(0)4
M3 - (90)4(0)4
N1 - (0)4(90)4(0)4
N3 - (0)4(90)4(90)4(0)4
M2 - (45)4(-45)4
M4 - (90)4(90)4

Fig. 8 95% confidence interval of the mean on all CFRP composites (M, N, O)

A. COHESIVE INTERLAMINAR DEBONDING

B. EDGE PEEL PROPAGATION

C. MIXED INTRALAMINAR FAILURE
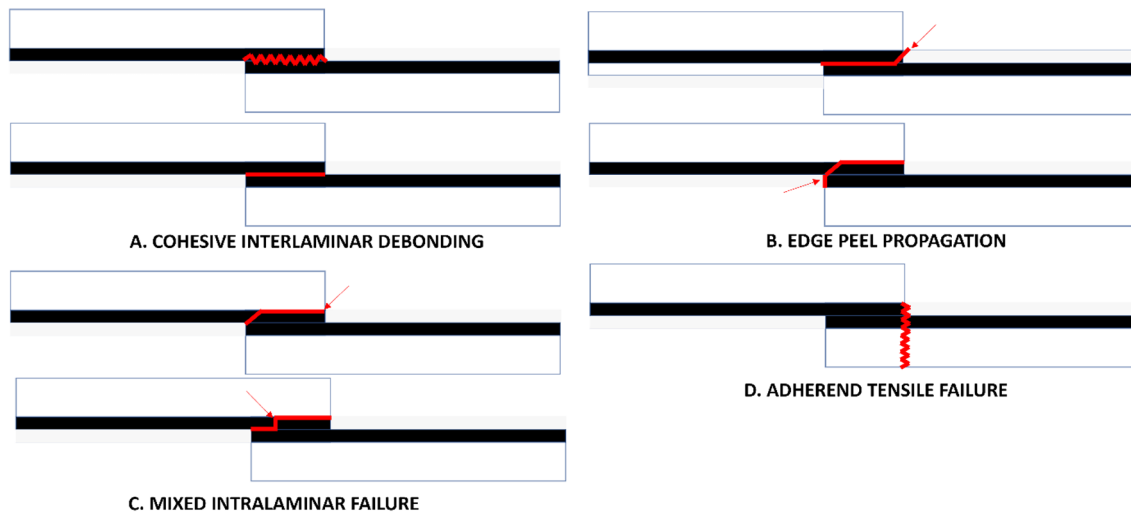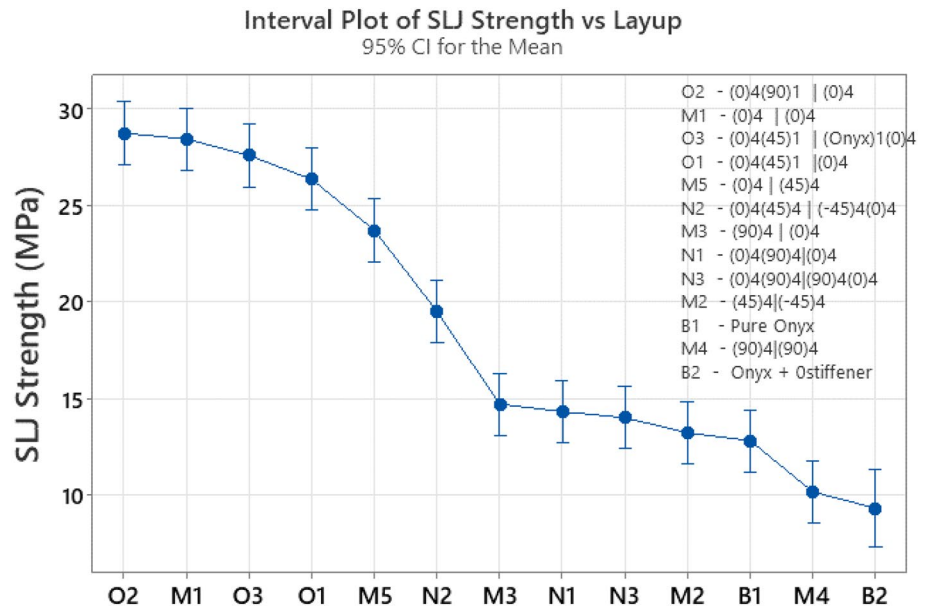
D. ADHEREND TENSILE FAILURE

Fig. 9 Failure mode determination of SLJ specimen (Adapted from [44])

edges of the lapped joint. Type C displays a lamina failure by tensile stresses, in which the failure scheme is almost certain to be the result of a combination with A or B. Type D displays an invalid test result where adherend tensile failure occurs. Fracture morphologies on the side of all SLJ specimens were identified and listed in Fig. 10. Detailed recognitions were done regarding the proposed identification scheme in Fig. 9.

Configurations of M1, N2, O1, and O3 have been recognized to fail within the centroid layer as they possess a balanced adherend stiffness, and the edges are not prone to mode II shearing as opposed to the specimens with a 90° ply. Configurations M2 and M4 were found to undergo intralaminar fracture within the four off-direction plies region,

which could result from a combination of peel and shear. As discussed later in section 4.5, it is evident that the lack of extensional stiffness would incur higher peel stresses. Configuration M3, M5, N1, N3, and O2 all have a failure occurring within the interlaminar 45°/90 layers potentially caused by the mixed loading of concentrated peel/shear stresses on the off-axis lamina. It is also possible that the modulus mismatch between the off-axis ply and the adjacent 0-degree layer induced additional interlaminar shear stress that promoted fracture.

The results of SLJ strength and failure mode recognition for group M, N, O, and B2 specimens were plotted in Fig. 11. Type A, B, and C were according to Fig. 9. The result is consistent with the shear strength value when the
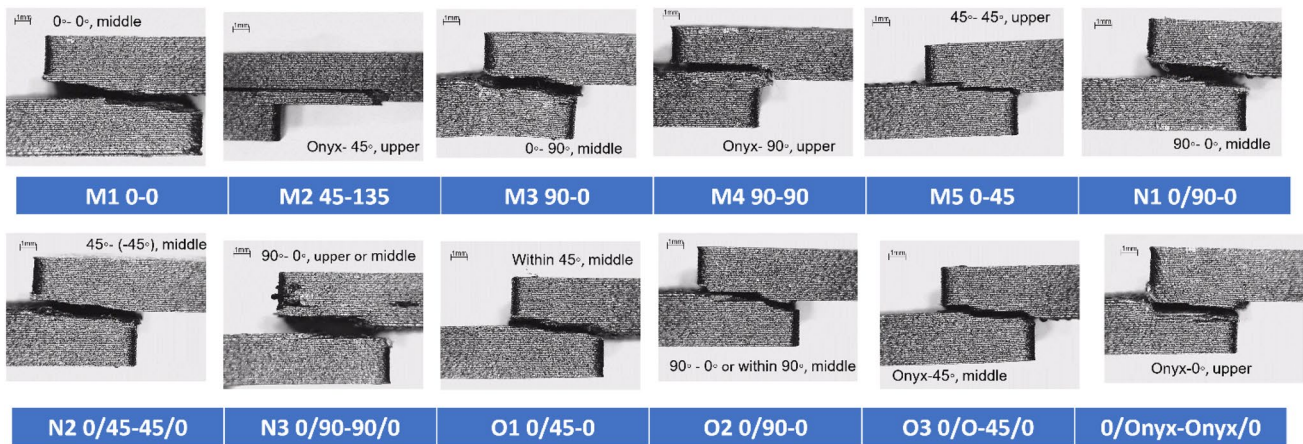
Fig. 10 Interlaminar fracture identification for all SLJ specimens

failure occurs within a non-0° layer. Decreased properties were observed when a layer of weak tensile strength was presented, namely in the 45° and the 90° layers. The failure on those specimens was caused by inadequate intralaminar bonding between each linear placement of directional fiber. Comparing the strength and fracture mode in M3, N1, and N3 shows an identical pattern for their similar composition of mismatched 0°–90° interface. Statistical treatment reveals that the variation among these three configurations is non-significant, which supports the claim that additional 0° stiffeners would not effectively reinforce the beam if the shear-dominated failure occurs. M2 and M4 specimens displayed the lowest SLJ strength amongst all the M, N, and O configurations. It is to say that a successive off-axis layer without unidirectional reinforcement could spur a structural weakness, especially when the off-axis load encounters them. The B2 sample of the Onyx at the interlaminar area with an additional 0° stiffener displays the lowest SLJ strength, resulting from failure between the Onyx and unidirectional 0°. It is concluded that delamination occurs on the B2 while undergoing eccentric loading.

Fracture propagation was observed to jump to the adjacent layer in specimens M1, M3, M5, N3, O2, and stiffened Onyx. Other than the weakness of interlaminar debonding, another probable reason is the defects embedded systematically along the extrusion tool path. The type B failure of crack propagation through the gap between the continuous fiber and the wall enclosures weakened the strength. The propagation might also be attributed to other intralayer defects induced by the printing process, such as void and unfilled regions. General fracture modes in SLJ specimens are cohesion, adhesive, or adherend failure, which can apply to the 3D printed composite sample within the scope of Fig. 9 for types A, C, and D, respectively. The fracture could occur along the eccentric load path, defined by the EC, to the intersection of the interlaminar bonding area.

The resulting stresses might also cause intralaminar failure upon encountering a weaker lamina. Identical failure modes were observed in N1 and N3. The additional 0° layer did not improve the structural integrity. Instead, it introduced more bending moments on the unsupported edges, which causes type B fracture propagation. Group O specimens were designed to test the interfacial strength between fiber layups with a near-symmetrical stiffened beam. Failure morphologies on the group O specimens shows that the stiffened beam can effectively resist peel-induced bending, keeping the load transfer properly on the single-lap joint. Although the additional interlaminar buffer layer of 45°, 90°, and 45°-Onyx were expected to provide additional strain energy releasing effect, the difference between the O specimens and M1 0–0 is not significant.

3.4 Stress field from FEA

The simulated results were grouped as their characteristics, namely symmetric, semi-symmetric, and asymmetric. The stress field data were probed at the interfacial element surfaces within the middle section of the overlap area between the two sets of the 4-ply laminated structure. The data presented are of the shear stresses acting along the shear-loaded XZ surfaces, as x is the longitudinal direction and z is the through-the-thickness direction. The flexible Onyx outermost walls were excluded from the probed region to avoid stress singularity, abrupt straining at the free edges, and the plastic spew effect stated in previous section. The nonlinear mechanical response of the matrix materials was modeled using an isotropic multilinear plasticity model by curve-fitting of the plasticity zone over the stress–strain curve of pure Onyx samples. The calibration process was done using the tensile data, following the instruction in the ANSYS manual [51]. The normalized stress distribution on configuration N2 using a 0.2 mm element size was plotted in Fig. 12, and the
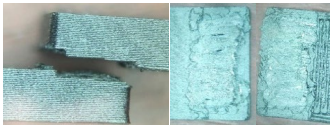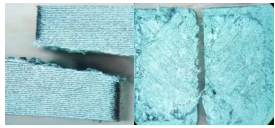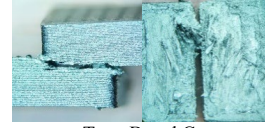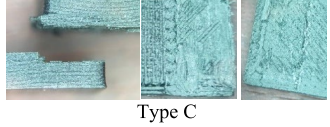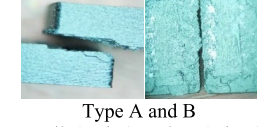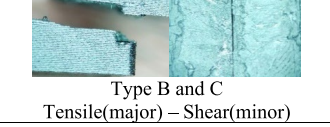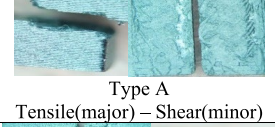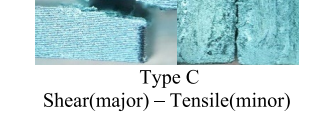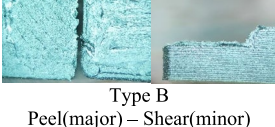
Sample	σ_{avg} (MPa)	Fracture surface morphology	Sample	σ_{avg} (MPa)	Failure surface morphology
M1 $(0)_4 - (0)_4$	28.5 ± 0.9	Type A and B Shear(major) − Tensile(minor)	N2 $(0)_4(45)_4 - (45)_4(0)_4$	19.5 ± 1.1	Type A Shear(major) − Peel(minor)
M2 $(45)_4 - (45)_4$	13.2 ± 1.6	Type C Tensile(major) − Peel(minor)	N3 $(0)_4(90)_4 - (90)_4(0)_4$	14.0 ± 2.1	Type B and C Shear(major) − Tensile(minor)
M3 $(0)_4 - (90)_4$	14.7 ± 1.1	Type A and B Shear(major) − Tensile(minor)	O1 $(0)_4(45)_1 - (0)_4$	26.4 ± 1.2	Type A and C Tensile(major) + Shear(minor)
M4 $(90)_4 - (90)_4$	10.2 ± 1.6	Type C Tensile(major) − Peel(minor)	O2 $(0)_4(90)_1 - (0)_4$	28.8 ± 0.8	Type A and B Tensile(major) + Shear(minor)
M5 $(0)_4 - (45)_4$	25.0 ± 2.2	Type B and C Tensile(major) − Shear(minor)	O3 $(0)_4(Onyx)_1 - (45)_1(0)_4$	27.6 ± 0.5	Type A Tensile(major) − Shear(minor)
N1 $(0)_4(90)_4 - (0)_4$	14.3 ± 0.6	Type C Shear(major) − Tensile(minor)	B2 Onyx + stiffener $(0)_4(Onyx)_4 - (Onyx)_4(0)_4$	9.3 ± 0.4	Type B Peel(major) − Shear(minor)

Fig. 11 Single-lap shear results for continuous fiber-reinforced composites with different fiber layups between adjacent interlaminar layers

resulting trend is identical to the distribution generated by analytical models [28, 32].

Four configurations were marked as symmetrical samples, including M1, M4, N3, and B1. The simulated shear stress distributions are presented in Fig. 13. The ILSS and peel stress distribution profile along the normalized distance from the interlaminar bonded lap between two configured fiber laminas were plotted in Fig. 14. The stress concentration factor was calculated by dividing the stress resultant at each location by the simulated average SLJ strength. It is observed that by introducing 0° unidirectional ply as reinforcement, the additional bending stiffness would allow the structure to reduce the stress concentration on the edges of the bonded region. The result of the N3 also shows that the shear stress distribution could be more homogeneous by blending the lamina layout with 0°–90° along the loading line. Although N3 has more evenly distributed shear stress, the concentrated peel stresses on the free edges result in structural weakness, and the corresponding SLJ shear stress of N3 is only at 30% of the M1 configuration. The result of asymmetrical and semi-symmetrical adherends was compiled and plotted in Figs. 15 and 16, respectively. The maximum shear stresses were observed in the vicinity of the interlaminar bonding edges, which are of opposite directions on two sides for some of the samples.

Fig. 12 The simulated normalized stress distribution along the normalized x location
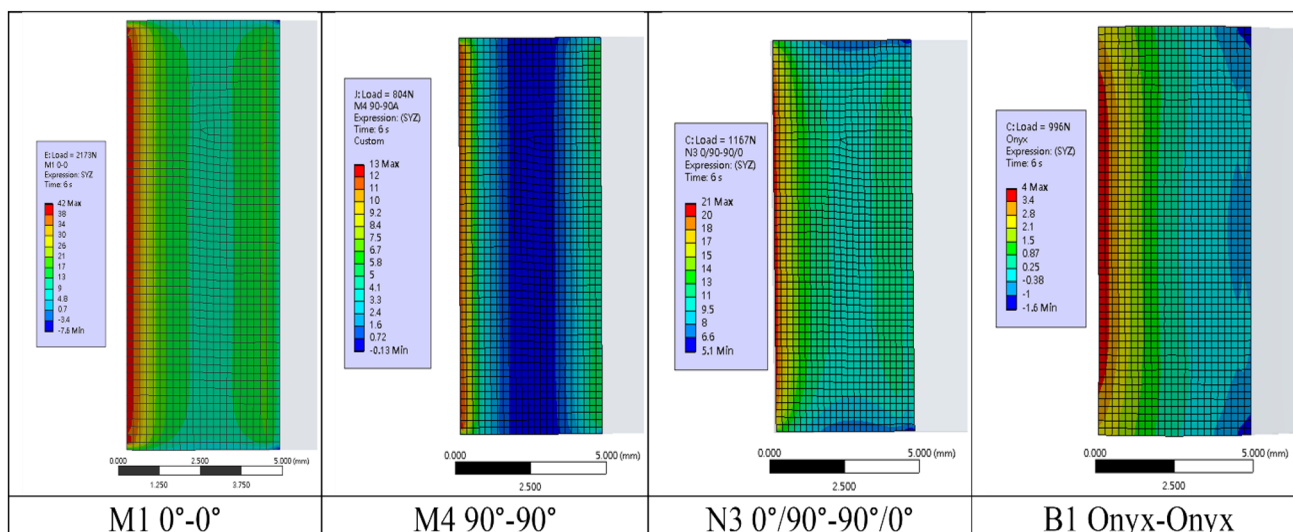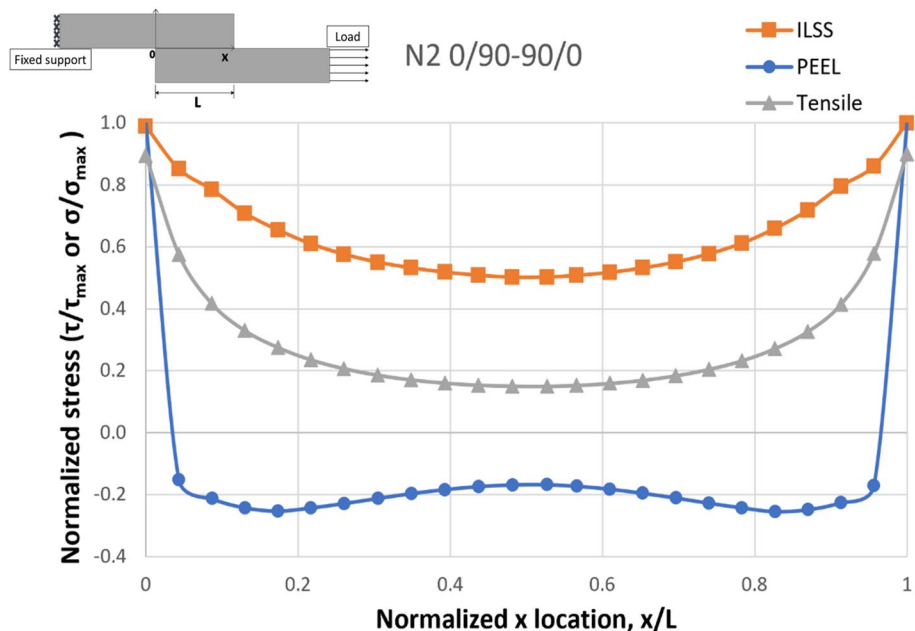

Fig. 13 FEA result of shear stress distribution—symmetrical adherends (unit: MPa)

A comparison of the simulated and calculated SLJ ILSS is plotted in Fig. 17. As mentioned in the earlier sections, SLJ failure is a combination of peel, shear, and tensile stresses resulting from the enforced tensile load. When the fracture is shear-dominated, a good correlation between the simulated and experimental results could be found. Shear-dominant failure is shown in N1, O1, and O2, for which the simulated average shear stresses at failure are almost identical to the estimated SLJ strength. For configurations where failure was not shear dominant, the calculated SLJ strength based on the average of an evenly distributed shear stress exceeded the simulated average. Examination of the stress components reveals the mixed stress failure behavior on each configuration, either tensile-peel dominant (M2, M4, N2, O3), tensile-shear dominant (M1, M3, M5, N1, N3), peel-shear dominant (N2, Onyx) or a mixture of the three (O1, O2).

4 Conclusion

The interlaminar shear strength of FFF composite samples and their failure behaviors were studied. A comparison of the results confirms that for additively manufactured
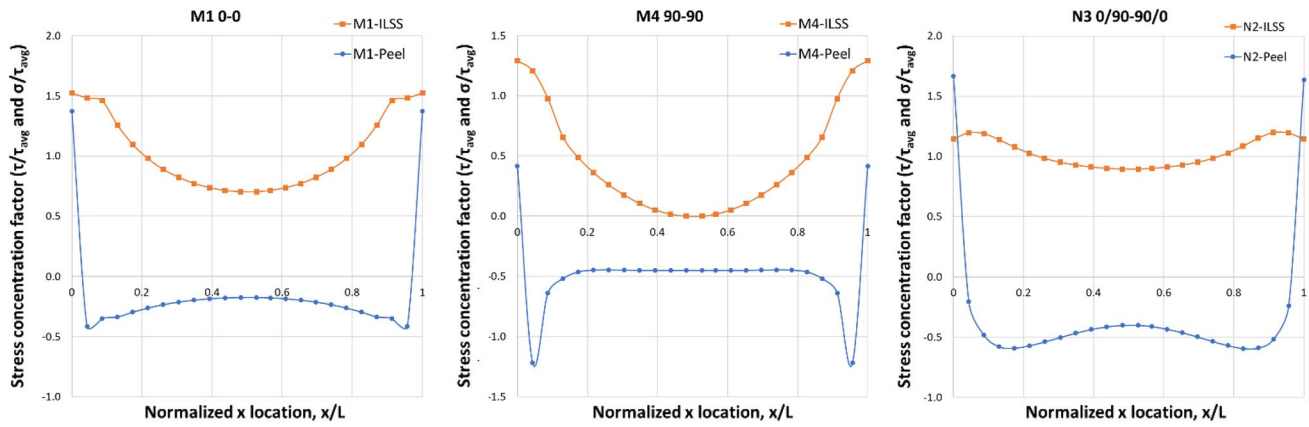
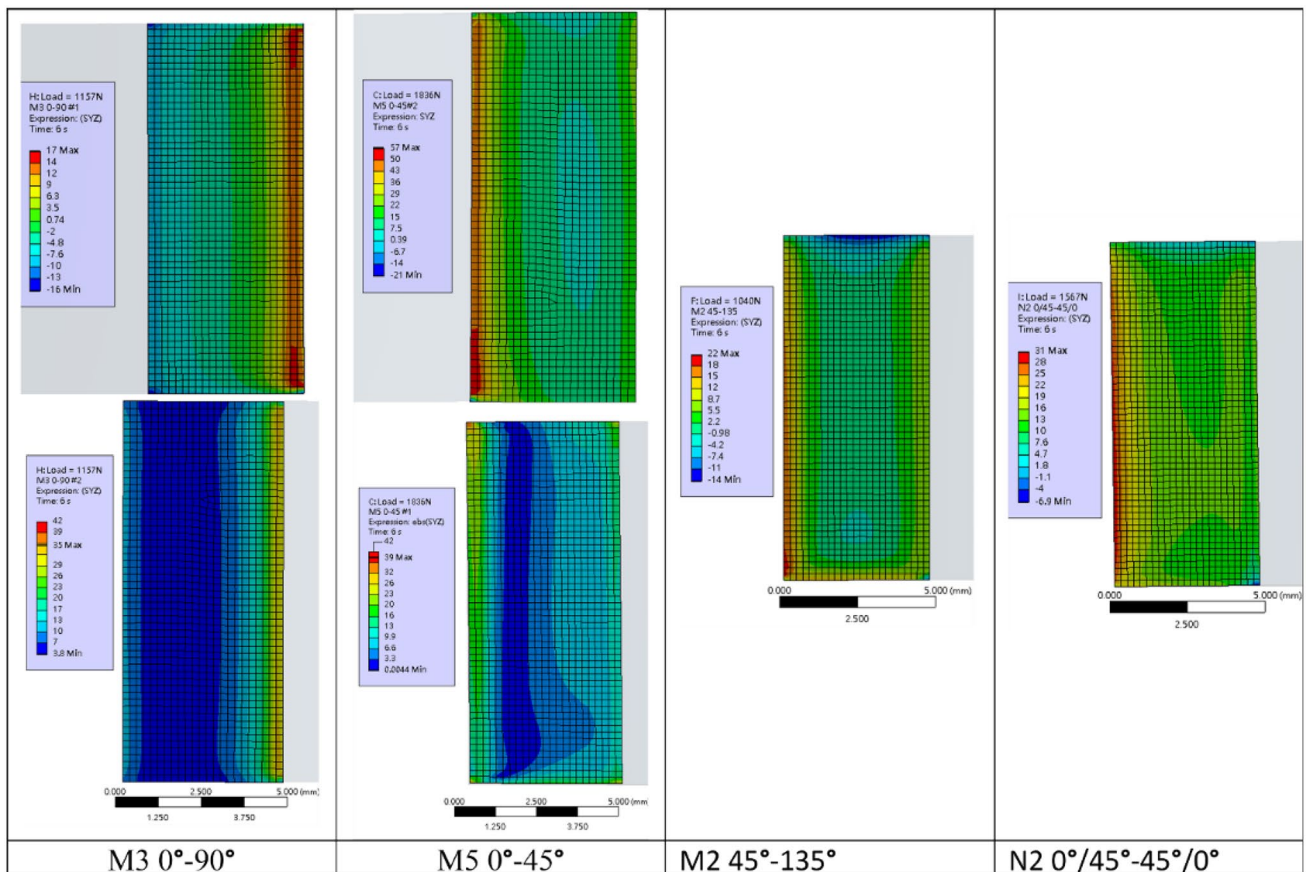**Fig. 14** Normalized stress distribution on CFRP samples with symmetrical adherends for ILSS and peel

Fig. 15 FEA result of shear stress distribution–asymmetrical adherends (unit: MPa)

CFRP, the structural inefficiency of the single-lap joint is still severe when the stiffer reinforcement is configured along the lap joint. This results from the peel stress introduced by the asymmetric stiffness, especially when interlaminar stresses are introduced by adjacent dissimilar plies resulting from the stiffness mismatch. This study has provided insight into the performance and primary modes of failure resulting from continuous reinforcement configurations on a 3D-printed functional part. Simply introducing unidirectional reinforcement of 0° increases the SLJ shear strength by more than twofold compared to the unreinforced Onyx specimens. It is also concluded that a consecutive directional 4-ply reinforcement seems insufficient to bear off-axis load for the induced risk of
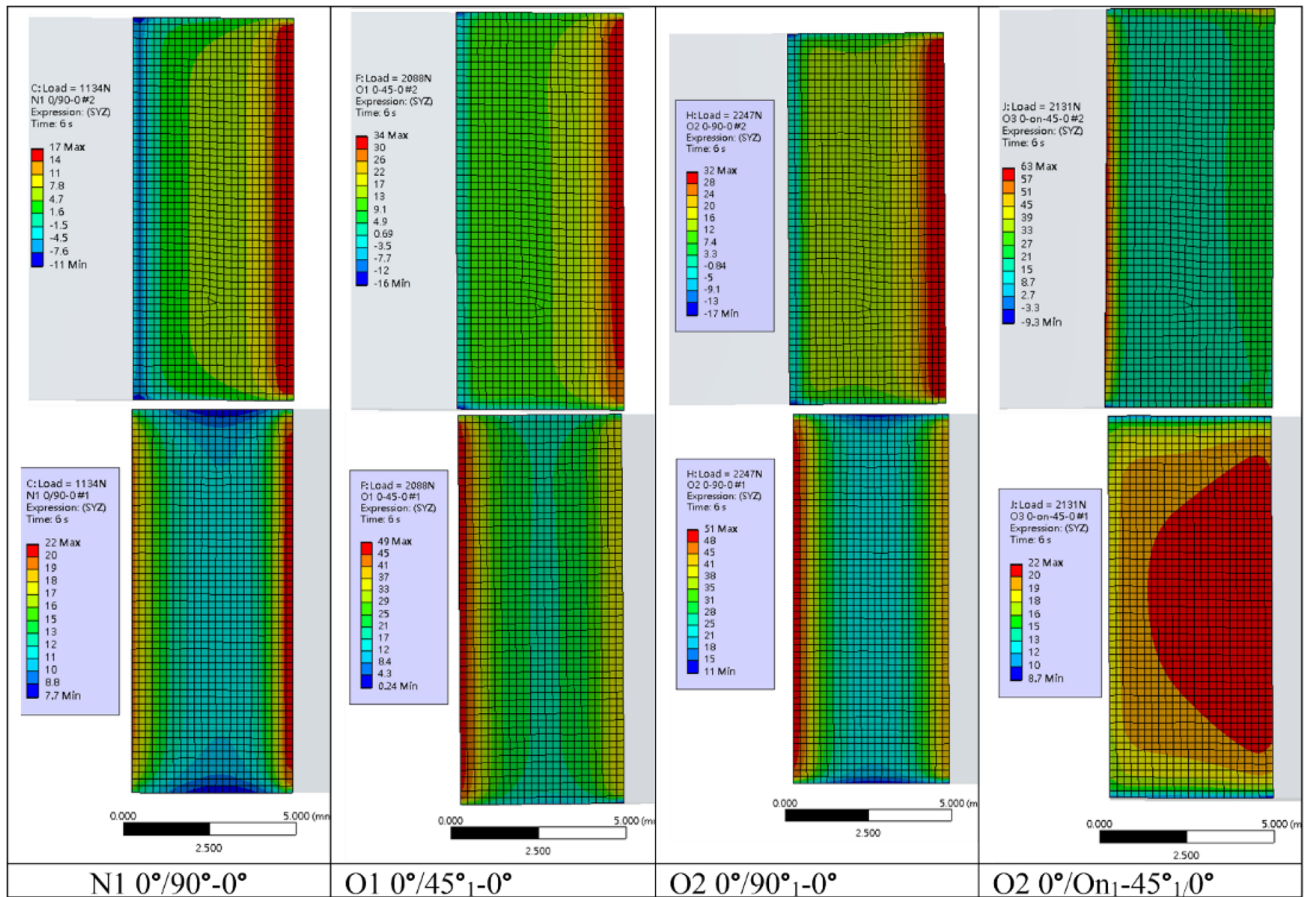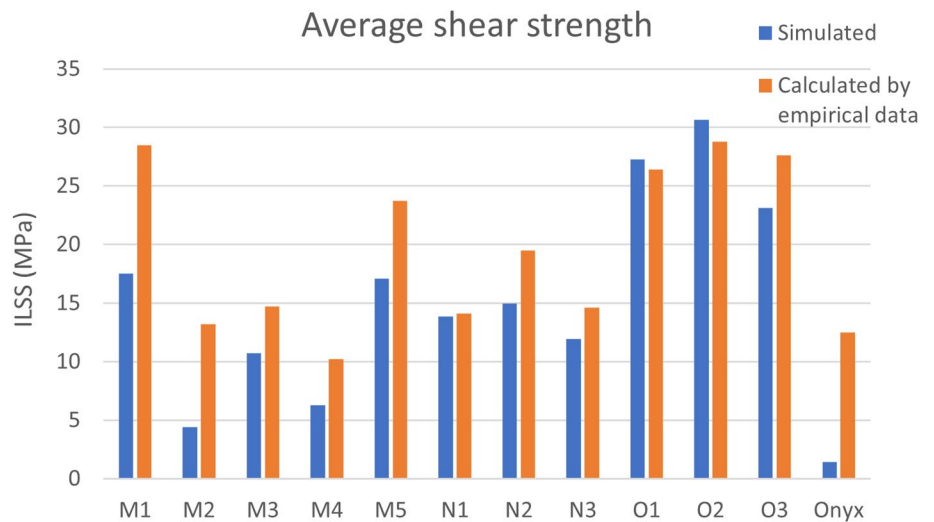
Fig. 16 FEA result of shear stress distribution–semi-symmetrical adherends (unit: MPa)

Fig. 17 Comparison of calculated and simulated average interlaminar shear stresses

delamination and heterogeneous stress distribution. It is recognized that the tested lap strength is a manifestation of a complex stress field for most configurations. The method presented here will be useful for ranking different 3D-printed reinforced configurations based on the interlaminar bonding quality.

Fracture morphologies were identified as a function of the corresponding dominant stress, namely shear, peel, and tensile stresses. It is essential to recognize the mode and to address a proper interpretation of the resulting SLJ stress accordingly. In addition, structural asymmetry of the lapped bodies is yet another factor that could cause unbalanced flexing. While comparing the group M and group N results, it became evident that the effect of the stiffness of the beam was more significant than the effect of fiber layups between directional plies. It is also found that the additional buffer layer cannot significantly strengthen the single-lap shear strength. Comparison within-group O shows the strength differences with the trend of $90° > Onyx-45° > 45°$. The result confirms that the implemented 45° layers are susceptible to composite loading of the shear-peel dominant condition. The trend also confirmed that a 90° layer could compensate for more property mismatch than a 45° layer. Inadequate bonding was identified between the Onyx-0° layer, Onyx-90° layer, and 45°–45° interfaces, as failure occurs in a low load in configurations M2, N2, N3, and B2. For FRPs, fiber layups between a near-symmetrical stiffened beam show a minor effect on the strength. 45° ply is not recommended because of weak inter-bead bonding that negatively affects the structural integrity of the printed composites and induces its susceptibility to shear and peel failure. It was established that limitations occur when the fulcrum-like edges and free edges cause stress concentration and a low-angle peel force.

This paper has demonstrated that the combination of results from a diversified experimental matrix and FEA simulation approach can provide a path for optimizing and ranking different reinforced AM configurations for achieving the best performance. FEA analysis was used to provide valid stress field information and details related to the failure mode for the AM composites. It is concluded that the load eccentricity can be precisely modeled with semi-implicit static structural FEA and provide relevant information on how the specimens were affected by the vertical stresses (peel stress) introduced by the flexing of the adherends and imbalanced stiffness. The overall trend suggests that characteristic printing pattern configurations can improve AM continuous fiber composite shear strength. Inserting a buffer layer of 90° or Onyx can improve the shear resistance of a unidirectional CFRP. A 45° layer may be included if the part undergoes off-axis direction loading to give a larger strain limit, while a consecutive 4-plies 45° or 90° laminate does not provide desirable strength under the SLJ setup. If applicable, an alternate layup sequence may provide a desired combination of shear strength and strain limit on the structure at the cost of ineffective tensile reinforcement. Examining the loading condition over an AM laminated composite is crucial because the highly nonuniform stress field could create unknown weaknesses if not carefully assessed. It is observed that even without considering the adhesive material in FEA, the stress profile is identical to the classical analytical treatment on the SLJ geometry.

Author contributions Y-CS (First author): conceptualization, data curation, methodology, validation, formal analysis, investigation, visualization, writing–original draft. HN (Corresponding author): conceptualization, formal analysis, writing–review and editing, resources, supervision, project administration. SS: conceptualization, supervision, formal analysis and writing. MM: data curation and investigation. JG: software, visualization, writing–review and editing. SP: supervision, resources, funding acquisition, writing–review and editing.

Data availability Testing data is available upon request.

Declarations

References

1. Ford SL (2014) Additive manufacturing technology: potential implications for US manufacturing competitiveness. J Int'l Com Econ 6:40

2. ASTM (2015) ISO/ASTM52900-15, standard terminology for additive manufacturing–general principles–terminology. ASTM International, West Conshohocken, PA. https://doi.org/10.1520/F3177-21

3. Hopkinson N, Hague R, Dickens P (2006) Rapid manufacturing: an industrial revolution for the digital age. John Wiley & Sons

4. Ngo TD, Kashani A, Imbalzano G, Nguyen KTQ, Hui D (2018) Additive manufacturing (3D printing): a review of materials, methods, applications and challenges. Compos B Eng 143:172–196. https://doi.org/10.1016/j.compositesb.2018.02.012

5. Han P (2017) Additive design and manufacturing of jet engine parts. Engineering 3:648–652. https://doi.org/10.1016/j.Eng.2017.05.017

6. Wragg NM, Burke L, Wilson SL (2019) A critical review of current progress in 3D kidney biomanufacturing: advances, challenges, and recommendations. Renal Replacement Therapy. https://doi.org/10.1186/s41100-019-0218-7

7. Klippstein H, De Cerio D, Sanchez A, Hassanin H, Zweiri Y, Seneviratne L (2018) Fused deposition modeling for unmanned aerial vehicles (UAVs): a review. Adv Eng Mater 20:1700552. https://doi.org/10.1002/adem.201700552

8. Goh GD, Toh W, Yap YL, Ng TY, Yeong WY (2021) Additively manufactured continuous carbon fiber-reinforced thermoplastic for topology optimized unmanned aerial vehicle structures. Compos Part B: Eng 216:108840. https://doi.org/10.1016/j.compositesb.2021.108840

9. Der Klift FV, Koga Y, Todoroki A, Ueda M, Hirano Y, Matsuzaki R (2016) 3D printing of continuous carbon fibre reinforced thermo-plastic (CFRTP) tensile test specimens. Open J Compos Mater 06:18–27. https://doi.org/10.4236/ojcm.2016.61003

10. Melenka GW, Cheung BKO, Schofield JS, Dawson MR, Carey JP (2016) Evaluation and prediction of the tensile properties of continuous fiber-reinforced 3D printed structures. Compos Struct 153:866–875. https://doi.org/10.1016/j.compstruct.2016.07.018

11. Dickson AN, Barry JN, McDonnell KA, Dowling DP (2017) Fabrication of continuous carbon, glass and Kevlar fibre reinforced polymer composites using additive manufacturing. Addit Manuf 16:146–152. https://doi.org/10.1016/j.addma.2017.06.004

12. Blok LG, Longana ML, Yu H, Woods BKS (2018) An investigation into 3D printing of fibre reinforced thermoplastic composites. Addit Manuf 22:176–186. https://doi.org/10.1016/j.addma.2018.04.039

13. Polyzos E, Katalagarianakis A, Polyzos D, Van Hemelrijck D, Pyl L (2020) A multi-scale analytical methodology for the prediction of mechanical properties of 3D-printed materials with continuous fibres. Additive Manuf 36:101394. https://doi.org/10.1016/j.addma.2020.101394

14. van de Werken N, Tekinalp H, Khanbolouki P, Ozcan S, Williams A, Tehrani M (2020) Additively manufactured carbon fiber-reinforced composites: state of the art and perspective. Additive Manuf 31:100962. https://doi.org/10.1016/j.addma.2019.100962

15. Kabir SMF, Mathur K, Seyam A-FM (2020) A critical review on 3D printed continuous fiber-reinforced composites: history, mechanism, materials and properties. Compos Struct 232:111476. https://doi.org/10.1016/j.compstruct.2019.111476

16. Iragi M, Pascual-González C, Esnaola A, Lopes CS, Aretxabaleta L (2019) Ply and interlaminar behaviours of 3D printed continuous carbon fibre-reinforced thermoplastic laminates; effects of processing conditions and microstructure. Additive Manuf 30:100884. https://doi.org/10.1016/j.addma.2019.100884

17. Gold SA, Strong R, Turner BN (2014) A review of melt extrusion additive manufacturing processes: I. Process design and modeling. Rapid Prototyp J 20:192–204. https://doi.org/10.1108/rpj-01-2013-0012

18. Herakovich CT (2012) Mechanics of composites: a historical review. Mech Res Commun 41:1–20. https://doi.org/10.1016/j.mechrescom.2012.01.006

19. Chawla KK (2012) Composite materials: science and engineering. Springer Science & Business Media, Berlin

20. Yavas D, Zhang Z, Liu Q, Wu D (2021) Interlaminar shear behavior of continuous and short carbon fiber reinforced polymer composites fabricated by additive manufacturing. Compos Part: B Engin 204:108460. https://doi.org/10.1016/j.compositesb.2020.108460

21. Yang C, Tian X, Liu T, Cao Y, Li D (2017) 3D printing for continuous fiber reinforced thermoplastic composites: mechanism and performance. Rapid Prototyp J 23:209–215. https://doi.org/10.1108/rpj-08-2015-0098

22. Caminero MA, Chacón JM, García-Moreno I, Reverte JM (2018) Interlaminar bonding performance of 3D printed continuous fibre reinforced thermoplastic composites using fused deposition modelling. Polym Testing 68:415–423. https://doi.org/10.1016/j.polymertesting.2018.04.038

23. He X, Ding Y, Lei Z, Welch S, Zhang W, Dunn M, Yu K (2021) 3D printing of continuous fiber-reinforced thermoset composites. Additive Manuf 40:101921. https://doi.org/10.1016/j.addma.2021.101921

24. Ghiasi H, Fayazbakhsh K, Pasini D, Lessard L (2010) Optimum stacking sequence design of composite materials part II: variable stiffness design. Compos Struct 93:1–13. https://doi.org/10.1016/j.compstruct.2010.06.001

25. Meyers MA, Chawla KK (2010) Mechanical behavior of materials. Cambridge University Press

26. Banea MD, da Silva LF (2009) Adhesively bonded joints in composite materials: an overview. Proceedings of the Institution of Mechanical Engineers, Part L: Journal of Materials: Design and Applications 223:1–18

27. Tsai MY, Morton J (1994) An evaluation of analytical and numerical solutions to the single-lap joint. Int J Solids Struct 31:2537–2563. https://doi.org/10.1016/0020-7683(94)90036-1

28. ASTM (2016) D4896–01 standard guide for use of adhesive-bonded single lap-joint specimen test results. ASTM International, West Conshohocken, PA. https://doi.org/10.1520/d4896-01r16

29. Goland M, Reissner E (1944) The stresses in cemented joints

30. Volkersen O (1938) Die Nietkraftverteilung in zug-beanspruchten Nietverbindungen mit konstanten Laschenquer-schnitten. Luftfahrtfor schung 15:41–47

31. Hart-Smith LJ (1973) Adhesive-bonded single-lap joints. National Aeronautics and Space Administration

32. da Silva LFM, das Neves PJC, Adams RD, Spelt JK (2009) Analytical models of adhesively bonded joints—part I: literature survey. Int J Adhesion Adhesives 29:319–330. https://doi.org/10.1016/j.ijadhadh.2008.06.005

33. da Silva LFM, das Neves PJC, Adams RD, Wang A, Spelt JK (2009) Analytical models of adhesively bonded joints—part II: comparative study. Int J Adhesion Adhesives 29:331–341. https://doi.org/10.1016/j.ijadhadh.2008.06.007

34. Kendall K (1975) Crack propagation in lap shear joints. J Phys D Appl Phys 8:512

35. Kupski J, Teixeira de Freitas S, Zarouchas D, Camanho PP, Benedictus R (2019) Composite layup effect on the failure mechanism of single lap bonded joints. Compos Struct 217:14–26. https://doi.org/10.1016/j.compstruct.2019.02.093

36. Kupski J, Teixeira de Freitas S, Zarouchas D, Benedictus R (2020) On the influence of overlap topology on the tensile strength of composite bonded joints: single overlap versus overlap stacking. Int J Adhesion Adhesives. https://doi.org/10.1016/j.ijadhadh.2020.102696

37. Peng X, Zhang M, Guo Z, Sang L, Hou W (2020) Investigation of processing parameters on tensile performance for FDM-printed carbon fiber reinforced polyamide 6 composites. Compos Commun 22:100478. https://doi.org/10.1016/j.coco.2020.100478

38. Kovan V, Altan G, Topal ES (2017) Effect of layer thickness and print orientation on strength of 3D printed and adhesively bonded single lap joints. J Mech Sci Technol 31:2197–2201

39. Falck R, Goushegir SM, dos Santos JF, Amancio-Filho ST (2018) AddJoining: a novel additive manufacturing approach for layered metal-polymer hybrid structures. Mater Lett 217:211–214. https://doi.org/10.1016/j.matlet.2018.01.021

40. Parandoush P, Tucker L, Zhou C, Lin D (2017) Laser assisted additive manufacturing of continuous fiber reinforced thermoplastic composites. Mater Des 131:186–195. https://doi.org/10.1016/j.matdes.2017.06.013

41. da Silva LFM, Campilho RDSG (2012) Advances in numerical modelling of adhesive joints, pp 1–93. https://doi.org/10.1007/978-3-642-23608-2_1

42. ASTM (2014) Standard D3165–07 standard test method for strength properties of adhesives in shear by tension loading of single-lap-joint laminated assemblies. ASTM International, West Conshohocken, PA. https://doi.org/10.1520/D3165-00

43. ASTM (2004) Standard D1002–01 standard test method for apparent shear strength of single-lap-joint adhesively bonded metal specimens by tension loading (Metalto-Metal). ASTM International, West Conshohocken, PA. https://doi.org/10.1520/D1002-01

44. D-99 A (2012) ASTM D5573 Standard practice for classifying failure modes in fiber-reinforced-plastic (FRP) joints. ASTM International, West Conshohocken, PA, 15, 2002. https://doi.org/10.1520/D5573-99R19

45. Reddy J, Robbins Jr D (1994) Theories and computational models for composite laminates
46. Hart-Smith L (2002) Expanding the capabilities of the ten-percent rule for predicting the strength of fibre–polymer composites. Compos Sci Technol 62:1515–1544
47. Díaz J, Romera L, Hernández S, Baldomir A (2010) Benchmarking of three-dimensional finite element models of CFRP single-lap bonded joints. Int J Adhes Adhes 30:178–189. https://doi.org/10.1016/j.ijadhadh.2009.12.005
48. Silva MRG, Marques EAS, Silva LFMD (2016) Behaviour under impact of mixed adhesive joints for the automotive industry. Latin American J Solids Struct 13:835–853. https://doi.org/10.1590/1679-78252762
49. Marques EAS, da Silva LFM, Flaviani M (2015) Testing and simulation of mixed adhesive joints for aerospace applications. Compos B Eng 74:123–130. https://doi.org/10.1016/j.compositesb.2015.01.005
50. Pipes RB, Pagano N (1994) Mechanics of composite materials. Springer, Berlin, pp 234–245
51. ANSYS I (2020) ANSYS mechanical APDL, Release 2020 R1, Help system, Theory Reference